ACS OMEGA

Article

Cite This: ACS Omega 2019, 4, 5496−5508

http://pubs.acs.org/journal/acsodf

Three-Dimensional Hybrid Mesoporous Scaffolds for Simvastatin Sustained Delivery with in Vitro Cell Compatibility

Zulema Vargas-Osorio,[†] Asteria Luzardo-Álvarez,[§] Yolanda Piñeiro,*[,†] Carlos Vázquez-Vázquez,[‡] J. Luis Gómez-Amoza,[§] José Blanco-Méndez,[§] Francisco J. Otero Espinar,[§] and José Rivas[†]

[†]Department of Applied Physics, Faculty of Physics, Lab of Nanotechnology and Magnetism (NANOMAG), Research Technological Institute, [‡]Department Physical Chemistry, Faculty of Chemistry, Lab of Nanotechnology and Magnetism (NANOMAG), Research Technological Institute, and [§]Department of Pharmacy and Pharmaceutical Technology, Faculty of Pharmacy, Universidade de Santiago de Compostela, E-15782 Santiago de Compostela, Spain

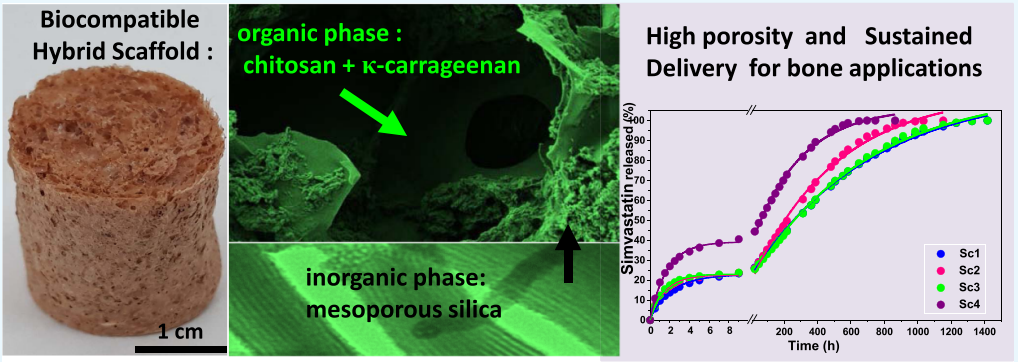

ABSTRACT: The development of scaffolds with suitable physicochemical and mechanical properties allowing for the structural regeneration of injured bone and recovery of the natural biological functionality is still a challenge in the tissue engineering field. Nanostructured materials with added theranostic abilities, together with an interconnected hierarchy of pores, offer the possibility to provide a new generation of bone implants. In this work, scaffolds with highly porous and resistant three-dimensional structures have been successfully developed by homogeneously embedding mesoporous silica nanostructures in a bioactive matrix of chitosan/κ-carrageenan. Moreover, magnetite (Fe_3O_4) nanoparticles were also added to the mesoporous scaffold to include additional magnetic functionalities for diagnostic or therapeutic actions. The complete physicochemical characterization shows mesoporous materials with a wide range of interconnected pores, remarkable surface roughness, and large effective surface area, suitable for cell adhesion. In accordance to these properties, a simvastatin loading and release assay showed high loading capacities and sustained release over a long period of time. Together with a suitable resistance against degradation and biocompatible performance assessed by cell viability assays, these scaffolds show interesting features for delivering drugs with activity in bone regeneration processes.

INTRODUCTION

Bone tissue defects caused by trauma, injuries, tumors, congenital deformities, and diseases often result in a surgical intervention and, in most cases, require the use of a type of bone graft when these are large enough or critical-sized.[1,2] The development of biomaterials capable of providing bone tissue regeneration and the recovery their biological functionality are becoming an area of growing interest to improve life quality of patients.[3,4] In this context, highly porous biocompatible scaffolds are intensively studied because of their ability to guide the growth of new tissue and stimulate specific cellular responses at molecular level.[5] Specifically, hybrid scaffolds composed of organic and inorganic biomaterials present the advantage of combining a balanced set of properties such as degradability and mechanical strength or flexibility and cohesion, to improve their biological functions.[6,7] From the list of bioactive and resorbable biopolymers used in tissue engineering, chitosan[8,9] is at the forefront of many pharmaceutical formulations for accelerated wound healing because of its antibacterial, haemostatic, and mucoadhesive power. In combination with the right amount of κ-carrageenan,[10] a negatively charged hydrophilic polysaccharide capable of forming high-strength elastic hydrogels, a porous scaffold can be obtained with a geometrically intricate architecture[11] that facilitates the formation of biosimilar grafts.[12]

Further incorporation of an inorganic phase to the polymeric matrix such as mesoporous silica material provides new functionalities that improve the overall performance to optimize the cellular scaffolding.[13] Ordered mesoporous silica

Received: December 30, 2018
Accepted: February 22, 2019
Published: March 19, 2019

DOI: 10.1021/acsomega.8b03676
ACS Omega 2019, 4, 5496−5508

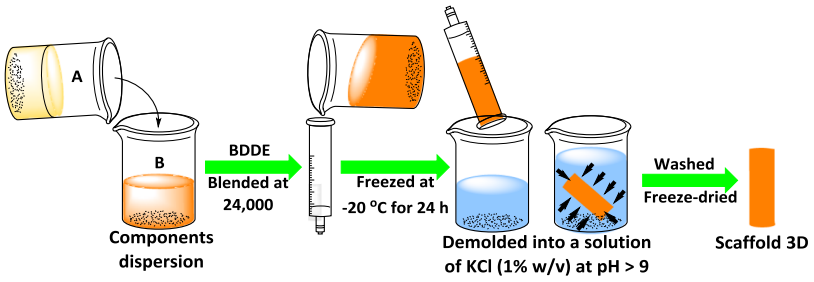

Figure 1. Synthesis of the 3D hybrid mesoporous scaffolds. A solution of κ-carrageenan in water (A) is added to a slightly acidic solution containing chitosan and SBA-15 mesoporous silica nanostructures (B) and blended at 24 000 rpm for homogenization. Next, BDDE is added under continuous blending, and this homogenized mixture is poured within a 10 mL syringe and kept at −20 °C for 24 h. Afterward, the cross-linking reaction is carried out by demolding the cylinder into a basic KCl solution at 60 °C for 24 h. Finally, the sample is washed with water and freeze-dried.

Table 1. Description of the Developed Scaffold Samples, Names (First Raw), and Their Mesoporous Silica Materials Content (from Second to Last Raws)

sample	formula	SBM[a]	characteristics	synthesis method	refs
Sc1	SBA-15	S15	ordered mesoporous silica	soft template	31
Sc2	SBA-15/Fe_3O_4@SiO_2[b]	LMNC	low magnetic content nanocomposite	microemulsion	22
Sc3	SBA-15/Fe_3O_4@SiO_2[b]	HMNC	high magnetic content nanocomposite	microemulsion	22
Sc4	SBA-15/Fe_3O_4@PAA[c]	$S15M_{PAA}$	magnetic mesoporous nanocomposite	coprecipitation	31

[a]Silica-based materials that are included the magnetic mesoporous nanocomposites. [b]Magnetite NPs Fe_3O_4 attached to the external SBA-15 surface by covering with a silica SiO_2 ultrathin layering. [c]Magnetite NPs functionalized with polyacrylic acid synthesized in situ in the presence of the SBA-15 material.

are known as third-generation biomaterials[14] that combine chemical, thermal, and mechanical stability, a hexagonal arrangement of pore channels (SBA-15-type mesoporous silica) together with a large and versatile surface that can be easily functionalized by silanol chemistry.[15,16] These materials are capable of loading large amounts of therapeutically relevant molecules such as peptides, enzymes, growth factors, antibodies, or genetic components[17] and provide local and steady release.[18] Moreover, nanosized mesoporous particles can be conjugated to antibodies[19] or functionalized with a fluorescent moiety[20] to be used in specific cell targeting or cell labeling applications. When, in addition, magnetite (Fe_3O_4) nanoparticles (NPs) are incorporated to produce magnetic mesoporous nanocomposites (SBA-15@Fe_3O_4), magnetic functionalities are added to the three-dimensional (3D) scaffolds. Magnetic doping provides synergistic effects such as bone regeneration through magnetic stimulation or adds theragnostic abilities such as MRI[21] or magnetic hyperthermia.[22] Recent innovations in bone tissue engineering have shown that magnetic scaffolds in combination with static magnetic fields are capable to improve bone cell migration, adhesion, proliferation, and growth.[23,24]

Finally, an appropriate drug selection can provide important therapeutic benefits when it is slowly released for a prolonged period from the scaffold. According to this, simvastatin is a popular cholesterol-lowering statin that has demonstrated positive effects in the bone regeneration process,[25−27] increasing the synthesis of bone morphogenetic protein 2 which is responsible for new bone formation, stimulating osteoblast proliferation, differentiation, and maturation.[28] Its participation in osteocalcin production and bone mass increase[29,30] has a bone protect effect, reducing fracture risk.

In this work, we have developed 3D mesoporous scaffolds by homogeneously blending an adequate proportion of inorganic mesoporous silica nanostructures (SBA-15 type) with a mixture of resorbable and bioactive natural polysaccharides, chitosan/κ-carrageenan, using a simple mixing and processing technique. The so-obtained structures were submitted to structural, morphological, and textural characterizations, showing a high degree of porosity with a random arrangement of voids, resistance to degradation, and capacity of loading large amounts of simvastatin together with a sustained and prolonged release for nearly 2 months.

Biocompatibility was assessed by WST-1 and neutral red cytotoxicity tests showing no toxic response, for plain scaffolds, whereas simvastatin-loaded materials showed an enhanced cell proliferation.

MATERIALS AND METHODS

κ-Carrageenan (Gelcarin GP 812NF) was supplied by IMCD; chitosan (high molecular weight, deacetylated chitin) was provided by Sinochem Quingdao Co. Ltd.; hydroxyapatite was supplied by Fluka; 1,4-butanediol diglycidyl ether cross-linker (BDDE, >95%) and acetic acid (glacial, $CH_3CO_2H \geq 99.85\%$) were obtained from Aldrich; and simvastatin was obtained from Fagron Iberica. Milli-Q (Merck-Millipore) deionized water was used in all of the experiments. The other chemicals used in our experiments were of analytical reagent grade (supplied by Aldrich) and were used without further purification.

Preparation of 3D Scaffolds (κ-Carrageenan-Chitosan/SBA-15-Fe_3O_4). The development of a new generation of highly porous 3D mesoporous scaffolds was obtained by designing a facile method that allows generating a bioactive and stable microstructure that can favor cell colonization, adhesion, and growth as briefly described in the scheme of Figure 1. In this regard, 100 mg of κ-carrageenan was dissolved in 5 mL of deionized water at 70 °C under vigorous magnetic stirring, to form a viscous gel. On the other hand, a second dispersion was prepared by dissolving 300 mg of chitosan in 5

DOI: 10.1021/acsomega.8b03676
ACS Omega 2019, 4, 5496−5508

mL of a slightly acidic solution, followed by the addition of 340 mg of the corresponding SBA-15-based material (Table 1), which was incorporated by strong manual stirring. The SBA-15-based materials were previously synthesized and reported by Vargas-Osorio et al.[22,31] The κ-carrageenan solution was poured into the chitosan/mesoporous silica dispersion. The new mixture was blended with an Ultra Turrax T25 at 24 000 rpm until a homogeneous dispersion was observed. Then, 0.4 mL of BDDE was added as a cross-linking agent and blended again.

To form a cylindrical scaffold, the homogeneous mixture was deposited inside a 10 mL syringe and then introduced into a freezer at −20 °C. Once frozen, the scaffold was demolded and immersed in a basic solution of potassium chloride (1% w/v) at 50−60 °C for 24 h to achieve cross-linking. After this time, the scaffold was washed with distilled water and lyophilized to obtain the final product.

Morphological and Microstructural Characterization. The morphology of the scaffolds was characterized by scanning electron microscopy (SEM) using a Zeiss FE-SEM ULTRA Plus microscope, employing secondary electrons and operating at 5 kV. The microporosity of the scaffolds was analyzed by mercury intrusion porosimetry (MIP) in a Micromeritics' Autopore IV (Norcross GA, USA) using a 3 mL powder penetrometer, with working pressures in the 0.004−172.4 MPa range and an approximate weight of the samples of 0.25 g. Pore size distributions were employed to model and simulate the scaffolds' porous structure by using the PoreXpert 1.3 software (Environmental and Fluid Modelling Group, University of Plymouth, UK). Mesoporosity and specific surface area were estimated from N_2 sorption isotherms obtained from a Micromeritics ASAP 2000 instrument. Finally, the functional groups present in 3D scaffolds were identified by Fourier transform infrared spectroscopy (FTIR) in a Thermo Nicolet Nexus spectrophotometer using the attenuated total reflectance method.

Simvastatin Loading and Release Study. Scaffolds with diameter Ø = 1 cm and mass 100 ± 10 mg were immersed in 10 mL of a water/ethanol simvastatin solution (3 mg/mL). Simvastatin loading was carried out by incubating them at room temperature for 24 h under dark conditions. After that, the remaining solution was separated from the simvastatin-loaded scaffolds and they were carefully dried and frozen at −20 °C for 24 h. Before lyophilization, they were completely frozen using liquid nitrogen at −195.8 °C. The release study was performed using an incubator with an orbital shaker IKA KS 4000ic at 37 °C and 100 rpm. The simvastatin-loaded cylinders were immersed in a vial containing 4 mL of phosphate buffer (pH = 7.4) and kept under physiological conditions. At predetermined time intervals, the entire solution was withdrawn and immediately replaced with an equal volume of fresh soaking medium, maintaining the volume constant. The amount of simvastatin released was monitored by UV/vis spectrophotometry, measuring the absorbance values at the wavelength of 239 nm, which is the wavelength of maximum absorption for simvastatin. A standard calibration curve (absorbance vs concentration) at different concentrations of free simvastatin in phosphate-buffered saline (PBS) was previously performed for this purpose. The simvastatin absorbance profiles obtained both to generate the standard curve and to know the concentrations released from each scaffold corroborated that simvastatin kept its properties after lyophilization because no difference between patterns was observed.

Drug release profiles were fitted to a biphasic first-order kinetic model. In this model, the initial fast release phase is described by a first-order process related to the dissolution of the drug adsorbed in the surface of the macropores. The second release phase is also governed by a first-order desorption kinetics associated with the drug released from pores of the mesoporous silica materials. The total fitting equation is

$$F = F_B(1 - e^{-k_1 t}) + (1 - F_B)(1 - e^{-k_2 t})$$

where F is the total fraction of drug released at time t, F_B is the fraction of drug released in the first phase, k_1 is the release rate constant of the initial phase, and k_2 is the release rate constant of the second phase. A nonlinear least-squares regression method was used to fit the release data to the model equations using GraphPad Prism version 6.00 for Windows, GraphPad Software, San Diego, California, USA. To determine the concentration of simvastatin-loaded, it was necessary to carry out the release assay until no absorbance was observed. Furthermore, the degradation resistance of the scaffolds was indirectly studied by keeping them in PBS under physiological conditions until reaching 1500 h.

Cell Culture and Treatments. Mouse macrophage cell line RAW 264.7 was obtained from ECACC (UK). Macrophages were cultivated in Dulbecco's modified Eagle's medium (DMEM, Sigma-Aldrich, Spain), supplemented with 10% of inactivated fetal bovine serum (FBS) and 1% of antibiotic/antimycotic mixture consisting of 10 000 units/mL penicillin and 10 000 units/mL streptomycin in 0.85% saline (Chemicon International). Macrophages were cultured in a humidified 5% CO_2 atmosphere at 37 °C.

Preparation of Extracts. Disk specimens from scaffolds were weighted (200 mg; 1 cm diameter) and kept for incubation during 1, 7, and 14 days in a complete fresh cell culture medium (DMEM, supplemented with mM L-glutamine, 100 units/mL of penicillin, 100 mg/mL of streptomycin, and 10% FBS; 10 mL) for extraction in the cell incubator at 37 °C. After predetermined periods of time, extraction medium samples were filtered (sterile filter 0.22 μm, Millipore) and triplicate cultures were seeded in 96-well plates. Cells were maintained for 24 h for each treatment and then prepared for the cell proliferation assays.

Cell Proliferation Assay. Scaffolds' cytocompatibility was evaluated by two standard methods: the WST-1 assay and neutral red uptake test. For the WST-1 assay, cells were seeded in 96-well plates at a density of 15 000 cells/well in DMEM supplemented with 10% FBS and left overnight for attachment. Cell proliferation was determined using the WST-1 reagent (Roche Diagnostics) according to the manufacturer's protocol.

The neutral red uptake test was performed as follows: neutral red stock solution of 40 μg/mL was added to cell culture (10 000 cells/well) in 96-well plates overnight. A destain solution for neutral red (50% ethanol/49% deionized water/1% glacial acetic acid) was used. For quantifying the extracted neutral red, a calibration curve was included in each experiment.

The mean absorbance and standard deviation of three replicates containing the same extract from each scaffold were calculated and expressed as percentage of the absorbance obtained for the control wells (nontreated cells), considered as 100% if cell viability. A concentration of 10% sodium dodecyl

DOI: 10.1021/acsomega.8b03676
ACS Omega 2019, 4, 5496−5508

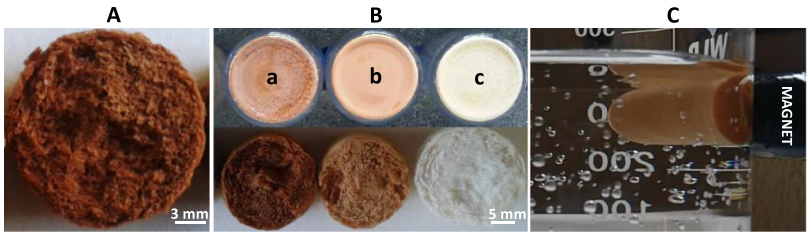

Figure 2. (A) Frontal view of a scaffold picture evidencing the wide range of porosity sizes observable at macroscopic length. (B) Upper raw corresponds to dried samples of mesoporous silica nanostructures doped with magnetite NPs; from right to left, samples color reflects the amount of magnetic NPs doping [(a) high amount of doping S15M$_{PAA}$, (b) medium doping LMNC, and (c) nondoped S15]. Bottom raw corresponds to the 3D hybrid mesoporous scaffolds prepared by mixing the mesoporous silica immediately above them, from right to left: in a Sc4-bottom is prepared with S15M$_{PAA}$, in (b) a Sc2-bottom is prepared with to LMNC, and (c) to Sc1-bottom is prepared with S15. (C) Magnetic response of the Sc2 cylinder in water under the action of an external neodymium iron boron permanent magnet.

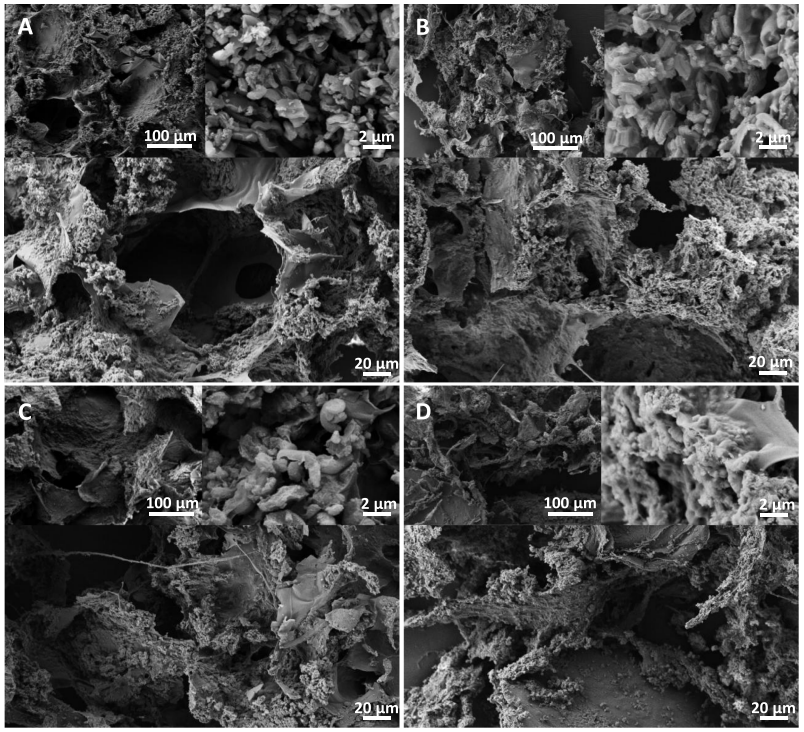

Figure 3. SEM micrographs at different magnification scales (100; 20; and 2 μm) of 3D hybrid mesoporous scaffolds (A) Sc1, (B) Sc2, (C) Sc3, and (D) Sc4, all evidencing the wide size range of pores in all of the prepared samples.

sulfate was used as negative control wells. Furthermore, the same assays were also performed only with simvastatin in solutions at 1, 10, 30, 50, and 100 μM. For better comparison, the cell viability results were rated relative to controls as: not cytotoxic (>90% viability), slightly cytotoxic (60−90% cell viability), moderately cytotoxic (30−59% cell viability), and strongly cytotoxic (<30% cell viability).[32]

Statistical Analysis. Data were expressed as mean ± standard deviation (triplicate samples). Statistical analysis was carried out using Student's two-tailed *t*-test. A *p*-value of <0.05 was considered to be statistically significant.

RESULTS AND DISCUSSION

The selection of chitosan and κ-carrageenan mixed with inorganic mesoporous silica matrices as components to develop a resistant biocompatible 3D porous microstructure is based on their chemical features that allow them to interact strongly. On one hand, the amines of chitosan behave as a reactive cationic polyelectrolyte with high charge density below pH 6.5,[33] easily adhering to the negatively charged κ-carrageenan molecules,[34] providing a high degree of mixing of both biopolymers. On the other hand, the additional incorporation of a cross-linker agent (BDDE) to the scaffold formulation and their submission to a basic-saline environment at 60 °C complete the covalent linking of the whole structure by ionic gelation, improving their stability and resistance, as was explained by De Boulle et al.[35] Additionally, another contribution to the porosity of these scaffolds arises during the freezing stage process in which small ice crystals are created that, on their turn, produce voids during the subsequent sublimation of the primary drying phase. The presence of mesoporous silica matrices inside the biopolymer structure further interferes with the ice crystal formation, contributing to the wide size range of porosity obtained.

The porous nature of the 3D hybrid mesoporous scaffolds is shown in Figure 2A,B. In Figure 2A, a frontal view of a scaffold shows that the cylindrical shape is preserved after the

DOI: 10.1021/acsomega.8b03676
ACS Omega 2019, 4, 5496−5508

demolding process and that the arrangement of pores is completely random. In Figure 2B, the upper raw corresponds to dried samples of mesoporous silica nanostructures doped with magnetite NPs; from right to left, samples color reflects the amount of magnetic NPs doping [(a) dark brown sample has a high amount of doping $S15M_{PAA}$, (b) light-orange has a medium amount of doping LMNC, and (c) nondoped S15H]. In Figure 2B, the bottom raw corresponds to the 3D hybrid mesoporous scaffolds prepared mixing with the mesoporous silica immediately above them, from right to left: in (a) Sc4-bottom is prepared with $S15M_{PAA}$, in (b) Sc2-bottom is prepared with LMNC, and (c) Sc1-bottom is prepared with S15H.

The color matching between the magnetically doped silica matrices and their scaffolds is due to the chemical stability of the covalent linking between magnetite NPs and mesoporous silica surface (SBA-15@Fe_3O_4) in accordance to prior studies reported by our group.[22] In Figure 2C, a magnetic scaffold sample (Sc2) cylinder, in water, is strongly attracted to the action of an external neodymium iron boron permanent magnet. It can be noticed that despite the sharp movement of the scaffold, the aqueous medium remains transparent and no leaching of magnetite NPs can be observed (Figure 2B).

The microstructure and morphology of the scaffolds were analyzed by SEM microscopy. Figure 3 shows highly porous hierarchical structures with a remarkable surface roughness and intricate pore walls. This special surface topography is given by the presence of the SBA-15-based material, which is uniformly distributed throughout the bioactive matrix. This silica component also contributed to generating pores with different morphologies and sizes, ranging from microns to nanometers and to creating a significantly interconnected structure. In this regard, the effects caused by this topography could have critical implications in bone regeneration, enhancing cellular function,[36] and increasing the initial attachment and seeding efficiency.[37]

High-magnification SEM images of Figure 4 display the interaction between the inorganic particles and organic phase. These particles are partially embedded by a polysaccharide film, which keeps them well integrated to the chitosan/carrageenan matrix. These images also evidenced the existence of a large interparticle porosity associated with pores of small sizes. Pores <3 μm can improve cell−surface interaction and anchorage-dependent cell−cell communication, as Bružauskaitė et al.[38] reported.

To precisely determine the different phases that constitute the 3D hybrid mesoporous scaffolds, a representative sample (Sc3) was analyzed by energy-dispersive system (EDS) mapping. Figure 5 shows two types of surface conformation, one enriched with magnetic SBA-15 mesoporous silica that increases and modifies the surface topography, making it irregular and intricate, and another flatter and smoother that corresponds to the chitosan/carrageenan matrix. By EDS mapping, the location of each chemical element along the scaffold can be identified, corroborating that the surface roughness is intimately related to the presence of rod-like mesoporous silica particles. Overall, the presence of carbon (C) and oxygen (O), main components of the polysaccharides, confirms that the organic part is the main constituent of the network. On the other hand, iron (Fe) from magnetite NPs appears in the same region as silica (Si), meaning that the magnetic mesoporous silica nanocomposite maintains its integrity during the scaffold production. In addition, sulfur

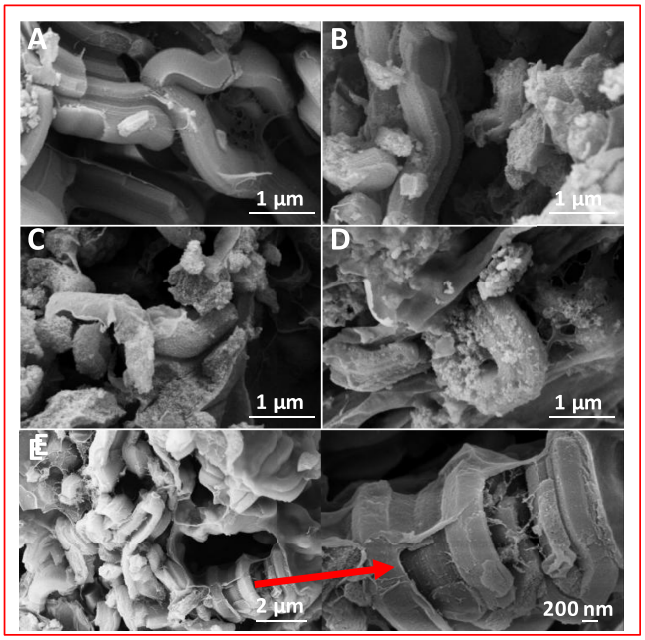

Figure 4. SEM micrographs of the 3D hybrid mesoporous scaffolds focused on locations where the embedded mesoporous silica nanostructures are clearly visible (A) Sc1, (B) Sc2, (C) Sc3, (D) Sc4, and (E) large magnification (200 nm) of a representative example that highlight the interaction between a SBA-15-based material and the chitosan/carrageenan phase, where some mesoporous particles are totally covered by the polymeric film.

(S), present in the linear sulfated κ-carrageenan, is mainly located in the same region where Fe appears, suggesting an intense interaction between magnetic nanocomposite (HMNC) and the polysaccharide.

The porous nature of the 3D mesoporous scaffolds was characterized by MIP and nitrogen sorption isotherms employing the Brunauer−Emmett−Teller (BET) and Barrett−Joyner−Halenda (BJH) methods. Their pore size distributions ranging from <0.1 to 200 μm are shown in Figure 6A. The addition of SBA-15-based materials played a crucial role in modifying the final features of the scaffolds. Comparing them to two scaffolds previously synthesized by Otero's group[39,40] from the same polysaccharide mixture one without any nanocomposite (ScPM) and another using hydroxyapatite (ScHA) instead. Only macropores between 10 and 200 μm were observed for ScPM, whereas for ScHA between 70 and 200 μm. Besides, both samples exhibited a low pore volume capacity. According to this, 3D hybrid mesoporous scaffolds display a significantly higher performance. Furthermore, these hybrid matrices also showed porosity at mesoscale. Thus, type IV isotherms with parallel adsorption and desorption branches associated with a type H1 hysteresis loop characteristic of the mesoporous materials with open cylindrical pores are displayed in Figure 6B. The pore diameter was calculated by the BJH method as is shown in Figure 6C, whose values are displayed in Table 2, exhibiting narrow pore size distributions with average pore sizes between 8 and 13 nm.

A detailed structural analysis of the scaffolds was performed by PoreXpert software using the experimental information obtained from MIP to calculate and create models with percolation characteristics similar to the studied materials. These models are represented by cubic structures, where the cubes correspond to pores and the cylinders to interconnec-

DOI: 10.1021/acsomega.8b03676
ACS Omega 2019, 4, 5496−5508

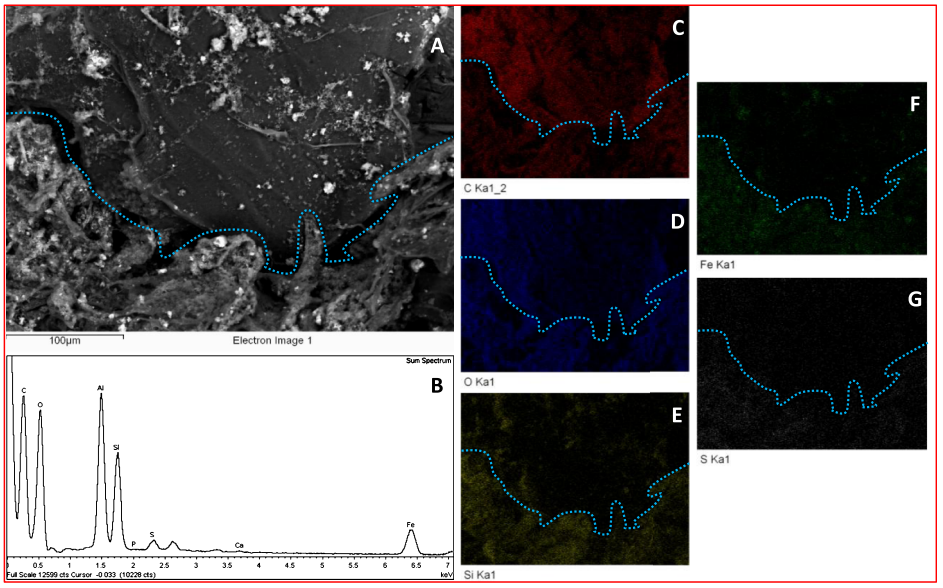

Figure 5. (A) SEM image, (B) EDS spectrum, and element mapping images for (C) C (red), (D) O (blue), (E) Si (yellow), (F) Fe (green), and (G) S (white) of the Sc3 hybrid mesoporous scaffold. The light blue line indicates an apparent separation between two different types of surfaces. (For interpretation of the references to color in this figure legend, the reader is referred to the web version of this article).

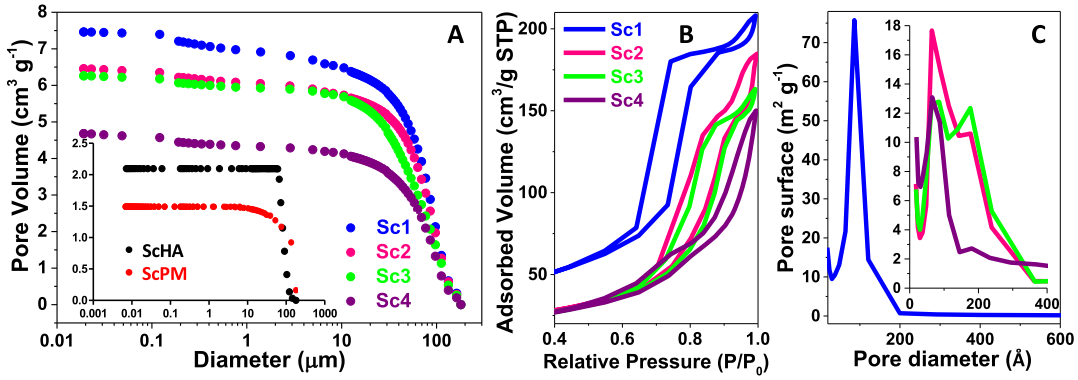

Figure 6. (A) Pore size distributions obtained from MIP of the 3D hybrid mesoporous scaffolds and the scaffolds previously synthesized by Otero's group,[39,40] (B) N_2 sorption isotherms analyzed by BET, and (C) pore size distributions calculated by the BJH method of the 3D hybrid mesoporous scaffolds.

Table 2. Textural Values Obtained From N_2 Sorption and MIP by Using the PoreXpert Software of the 3D Mesoporous Scaffolds

	N_2 sorption			MIP[a]					
samples	S_{BET} ($m^2\ g^{-1}$)	V_p ($cm^3 g^{-1}$)	D_{BJH} (nm)	porosity (%)	connectivity	correlation level	permeability (mD)	tortuosity	fluids absorption in 0.01 s (vol %)
Sc1	145.68	0.3080	8.46	83.77	3.90	0.161	2332.03	1.4	50.12
Sc2	80.10	0.2606	13.01	81.01	3.47	0.176	1882.39	1.6	56.81
Sc3	77.33	0.2403	12.43	81.52	3.80	0.262	980.20	1.6	58.82
Sc4	76.76	0.2085	10.87	78.96	5.82	0.166	3187.65	1.3	38.50

[a]The porosity percent is a direct measure of the fraction of void spaces volume over the scaffolds total volume. Connectivity refers to the number of pore channels connected to a node of the pore network. Correlation level determines the structural order or disorder of the pores (1 = high ordered porous structure and 0 = random distribution of the pores). Permeability is the ability to allow a fluid to cross the material without altering its internal structure. Tortuosity is a measure of the geometric complexity of a porous medium. The fluids absorption represents the volume percentage that has been filled with water after 0.01 s of being in contact with an aqueous fluid media.

tions. Table 2 compiles the estimated values of the hybrid mesoporous scaffolds; these results agree with those observed in SEM regarding highly porous and interconnected structures. These scaffolds possess a great capacity to absorb fluids without distorting their structure. Moreover, hybrid mesoporous scaffolds are partially ordered structures that are built up by disordered macropores and ordered mesopores. The previously obtained correlation levels and connectivity values of the ScHA and ScPM scaffolds below 0.01 and 2.6, respectively, demonstrated the presence of completely disordered and less interconnected porous structures. Figure 7 presents the 3D models generated by PoreXpert software of

DOI: 10.1021/acsomega.8b03676
ACS Omega 2019, 4, 5496−5508

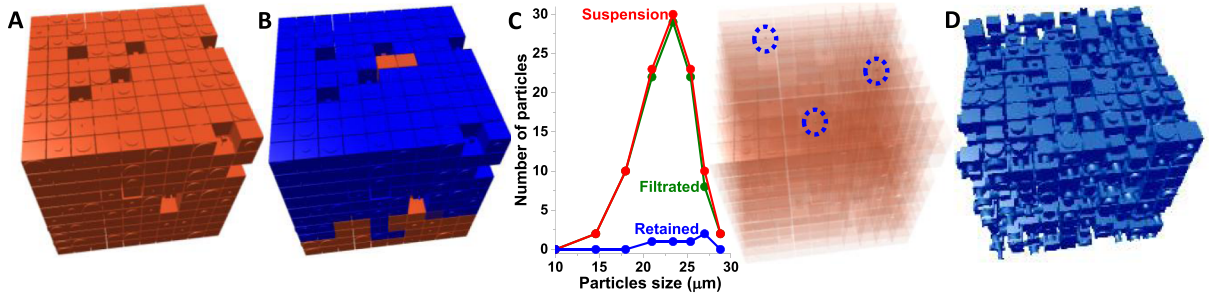

Figure 7. Cubic models created by PoreXpert software, showing the Sc1 scaffold features. (A) Almost perfect cube, which represents an extremely porous and interconnected structure, (B) volume of water capable of being absorbed per 0.01 s, and (C) simulation of bone cell migration by spreading spherical particles with diameters between 10 and 30 μm, equivalent to bone cells (i.e., osteocytes with 7 μm of width and depth, and 15 μm of length),[41] through the scaffold, where only a few particles with sizes higher than 20 μm remain trapped. (D) Porosity of the ScHA scaffold.

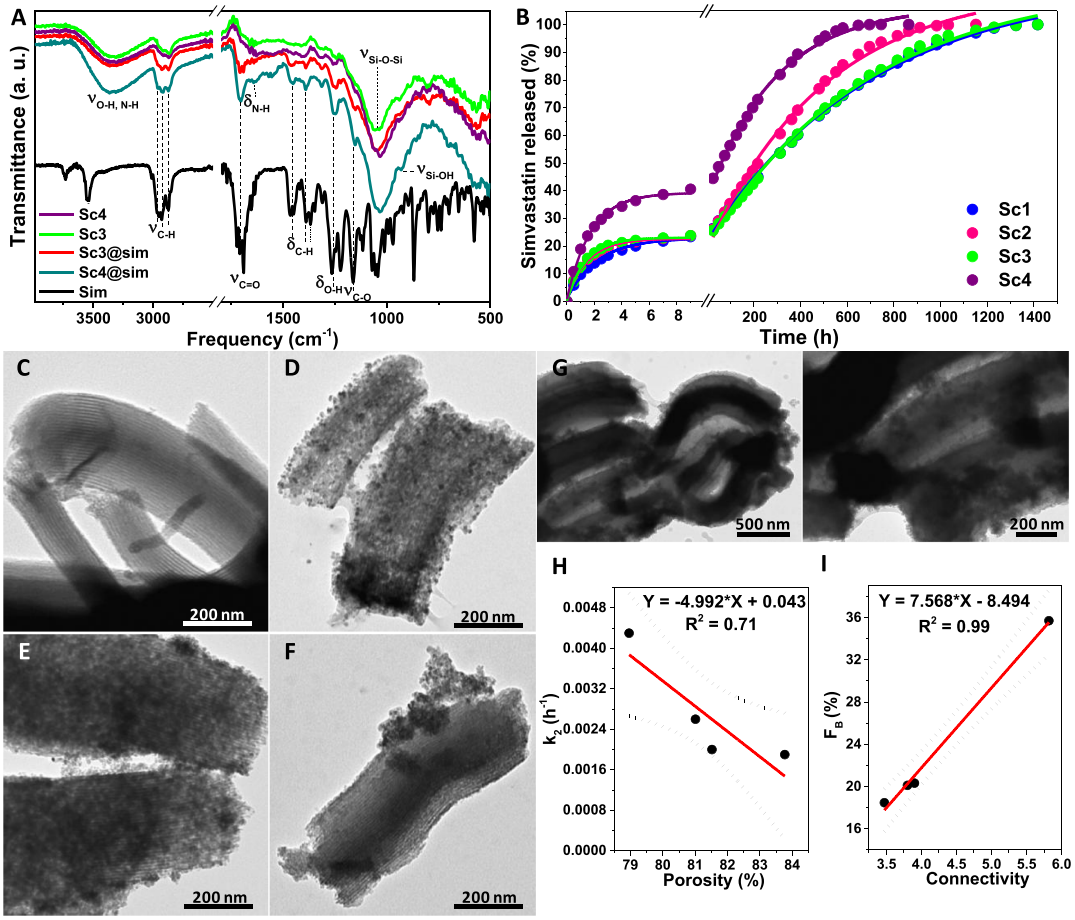

Figure 8. (A) FTIR spectra of simvastatin, loaded simvastatin, and plain mesoporous scaffolds, (B) simvastatin release profiles of the 3D hybrid mesoporous scaffolds, where lines represent the fitting models of the biphasic first-order kinetics, TEM micrographs of the 3D hybrid mesoporous scaffolds, where (C) corresponds to Sc1, (D) to Sc2, (E) Sc3, (F) Sc4, and (G) an example that best represent the interaction between organic and inorganic components (Sc4 scaffold), (H) linear relationship between connectivity and F_B, and (I) linear relationship between porosity and k_2.

the Sc1 scaffold and, additionally, the 3D model of the ScHA scaffold as the best previously synthesized sample.

Simvastatin Loading and Release Assay. The scaffolds were analyzed by FTIR to corroborate the adsorption of simvastatin. The spectra of two representative bare- and simvastatin-loaded scaffolds (Sc3, Sc4) are shown in Figure 8A, together with the characteristic pattern[42] of pure simvastatin for comparison purposes. It can be observed that in the loaded scaffold pattern, some of the characteristic peaks of simvastatin appear overlapped on the pattern of bare scaffolds. Specifically, this overlapping is evident through the intensification of asymmetric and symmetric C−H stretching bands and C−H bending vibrations at 2935 and 2872 cm^{-1} and at 1460 and 1370 cm^{-1}, respectively. However, the clearest signature of simvastatin presence is that associated with a high-intensity stretching vibration at 1709 cm^{-1}, corresponding to carbonyl functional groups, followed by a slight intense O−H deformation vibration, observed at 1250 cm^{-1}, and a small absorption band at 1158 cm^{-1} is assigned to the C−O stretching mode.

DOI: 10.1021/acsomega.8b03676
ACS Omega 2019, 4, 5496−5508

Table 3. Simvastatin Loading Capacity and Loading Efficiency and the Parameters Obtained by Fitting the Simvastatin Release Profiles to a Biphasic First-Order Kinetic Model[a]

sample	capacity (mg g^{-1})	efficiency (%)	Q_{9h} (mg)	F_B (%)	k_1 (h^{-1})	k_2 (h^{-1})	R^2
Sc1	236.2	78.6	5.97	20.32	0.576	0.0019	0.9964
Sc2	187.8	62.6	4.06	18.47	1.098	0.0026	0.9950
Sc3	213.4	70.9	5.48	20.11	0.967	0.0019	0.9950
Sc4	196.1	65.3	8.22	35.70	0.698	0.0043	0.9956

[a] Q_{9h} represents the amount of simvastatin delivered during the first 9 h; F_B corresponds to the fraction of simvastatin released in the first phase; k_1 and k_2 are the first-order rate constants of the first and second delivery stages, respectively; and R^2 is the coefficient of determination.

The simvastatin loading capacity and efficiency of the 3D hybrid mesoporous scaffolds are shown in Table 3. The simvastatin release profiles of Figure 8B display a biphasic behavior, which is related to a faster release rate during the first 9 h followed by a second stage governed by a much slower kinetics associated with a sustained release process. The second stage was performed over a long period, lasting between 700 and 1400 h. In this regard, the release profiles were perfectly fitted to a biphasic first-order kinetic model, obtaining coefficients of determination higher than 99.5%. The significant initial burst effect corresponded to the fast simvastatin dissolution and diffusion from macropores. This relatively fast release is supported by values of k_1 significantly higher than k_2, which agrees with the model proposed by Gallagher and Corrigan[43] for biodegradable drug delivery systems with an initial burst release. In contrast, the second release profile was controlled by a first-order kinetics associated with simvastatin desorption from mesopores, whose presence is evidenced by transmission electron microscopy (TEM) microscopy. Figure 8C−F reveals the presence of different SBA-15-based materials, which have an ordered mesoporous channel system and the attachment of magnetite NPs to the SBA-15 surface for the magnetic nanocomposites. Figure 8G best illustrates the interaction between rodlike particles and the bioactive polysaccharide matrix. In this regard, $S15M_{PAA}$ particles are completely embedded in the chitosan/κ-carrageenan mixture, forming a single system where all components are consistently integrated. On the other hand, linear correlations between some parameters were obtained. Figure 7C,D shows that an increase in connectivity is directly proportional to an increase in the percentage of simvastatin released during the first stage (F_B), whereas an increase in porosity produces a decrease in the second release constant (k_2). Thus, the release magnitude in the first stage depended on connectivity by facilitating drug diffusion, as well as a higher porosity allowed a better control over drug kinetics, where the pore size distribution is an important factor.

In addition, the differences in the release profiles are also associated with the lipophilic nature of simvastatin; thereby, the intermolecular interactions between the simvastatin and functional groups were stronger in those SBA-15 mesoporous silica nanostructures with a relatively hydrophobic surface such as Sc1, Sc2, and Sc3, which possess silanol groups (Si−OH), being Sc1 the sample with clearly the largest surface area. Furthermore, different magnetic mesoporous nanocomposites were employed for the synthesis of Sc2 and Sc3, where Sc3 has a higher amount of magnetite NPs incorporated, which could have increased the hydrophobicity in the medium. Therefore, Sc1 and Sc3 loaded the highest amount of simvastatin and present the slowest k_2 release constants and the most sustained releases.

In general, the use of mesoporous silica has drastically increased the loading capacity of the scaffolds, allowing them to adsorb large amounts of simvastatin compared to others. For example, the previously prepared ScHA scaffold[39,40] was loaded with ciprofloxacin instead of simvastatin, loading less than 7 mg g^{-1} and completely releasing it in 16 h. On the other hand, the ScPM scaffold was not able to adsorb more than 4 mg g^{-1} simvastatin (unpublished data). The advantages of the 3D hybrid mesoporous scaffolds as powerful sustained delivery systems were highlighted by comparing them with a recent article published by Yu et al.[44] related to a mesoporous hydroxyapatite/collagen scaffold that enhanced osteogenesis and angiogenesis by releasing simvastatin in a sustained way. Yu et al. obtained a simvastatin loading efficiency of 7.6% associated with a high loading concentration of 75.7 mg g^{-1} that was released over 500 h. In this regard, the results presented in our study demonstrate higher loading efficiencies, higher loading concentrations, and longer sustained delivery processes of simvastatin.

Degradability. Scaffold cylinders were immersed in simvastatin under physiological conditions (37 °C and 100 rpm) and kept for 1500 h, to test their stability in moisty environment for 3−4 weeks. After this short-term degradability test, mainly all scaffolds showed no morphological modifications or leakage of components. Previous 3D scaffolds based on natural polymer mixtures synthesized in our group (data not shown) with the aim of obtaining simultaneously good mechanic performance and sustained delivery profile allowed us to conclude that the absence of an inorganic component or mineral material inhibited the improvement of mechanical strength of the final formulations. On one hand, a mixture of alginate, gelatin, and κ-carrageenan, cross-linked for 24 h in a solution of $CaCl_2$ (1.5%) and glutaraldehyde (2.5%) at pH 7, was completely disintegrated in 48 h after having been immersed in PBS buffer. The rapid disintegration of the scaffold might be ascribed to an irregular and nonuniform cross-linking of the polysaccharides and the ionization of the κ-carrageenan and alginates at physiological pH causing the swelling and disaggregation of the system. This evidenced that mechanical performance of cross-linked alginate was worsened by the mixture. A further incorporation of other aqueous insoluble materials as zein, a hydrophobic vegetal protein that forms resistant aqueous insoluble aggregates, or chitosan was observed to slightly improve the mechanic properties without being able to stop disintegration in short periods of time. As Atila[45] mentioned, natural polymers based on fibrous scaffolds present an inadequate 3-dimensionality and poor mechanical properties for their use as bone substitutes, despite having excellent biocompatibility and bioactivity.

In fact, to overcome the lack of mechanical strength of chitosan-based scaffolds, many approaches have been made by combining chitosan with inorganic materials such as nano-

DOI: 10.1021/acsomega.8b03676
ACS Omega 2019, 4, 5496−5508

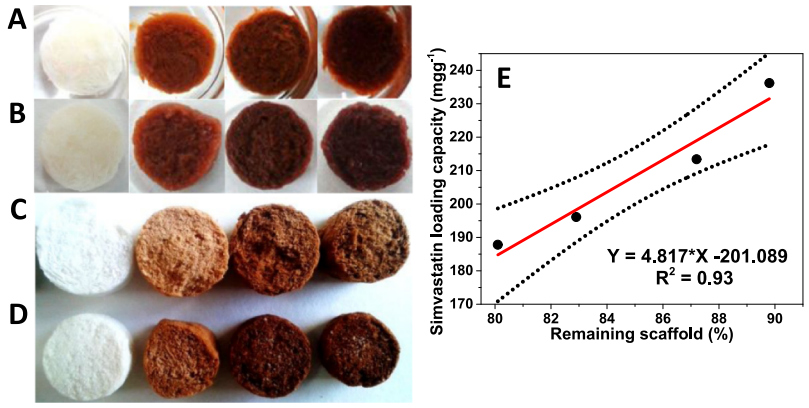

Figure 9. Appearance of the 3D mesoporous scaffolds after 1500 h of being under physiological conditions (37 °C and 100 rpm) (A) immersed in PBS, (B) outside PBS, (C) original lyophilized scaffolds, (D) final lyophilized samples, and (E) linear relationship between the percentage of the remaining scaffold and simvastatin loading capacity.

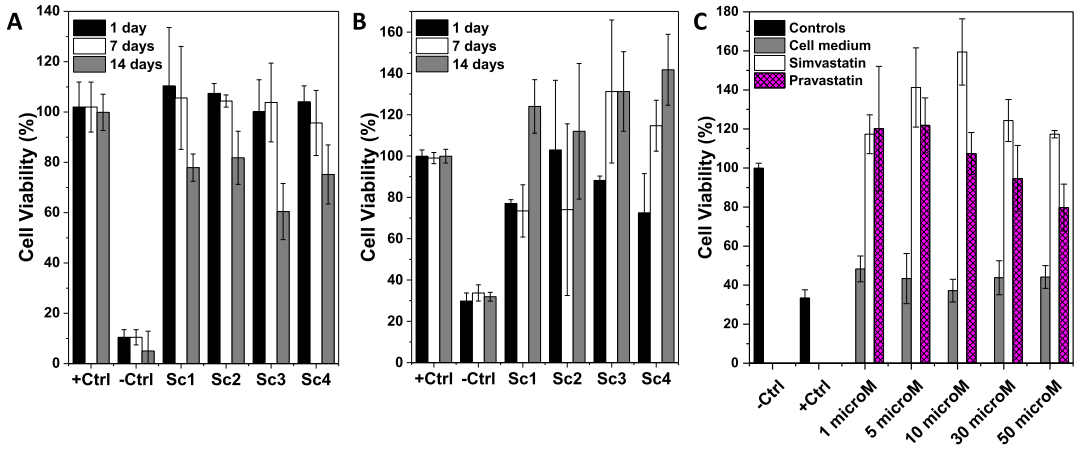

Figure 10. WST-1 results of cell viability corresponding to the fluid extracts obtained (A) from plain scaffolds (no simvastatin), (B) from simvastatin-loaded scaffolds, and (C) RAW 264.7 cell proliferation studies by WST-assay after incubation with simvastatin and pravastatin for 24 h.

hydroxiapatite,[46] silica,[47] or different ceramics or mesoporous silica,[48,49] which may or may not include drugs or biofactors. Conversely, κ-carrageenan has been scarcely used as a biomaterial, although its advantages and similarities to natural glycosaminoglycans present it as a candidate material to produce composite scaffolds when combined with mineral hydroxyapatite as bone substitutes.[50,51]

Thus, the incorporation of a SBA-15-based material to polysaccharides formulation determined its stability, increasing the mechanical properties of the hybrid scaffold. Figure 9 shows the appearance of the scaffolds after the assay was concluded, the scaffolds kept their cylindrical shape, whereas they were immersed in PBS, showing no signs of swelling. However, when Sc2 was set aside from buffer, a slight deformation associated with particle disaggregation was evidenced. Stability can also be related to scaffold fabrication, where a perfect homogenization of all constituents, avoiding the formation of bubbles during pouring and molding process is crucial. Finally, comparing the freeze-dried samples both the originals and those after 1500 h (Figure 8C,D), a slight contraction in all cases was observed, being the most radical that concerning to Sc2. In general, the materials were easy to handle and manipulate at any time, preserving between 90 and 80% of their original weight. Curiously, the scaffolds that remained in optimal conditions were those that loaded the highest amounts of simvastatin as is shown in Figure 8E. Therefore, the interactions that take place on the surface between the loaded molecules and functional groups of the scaffolds through interparticle forces seemed to have deep implications in the performance of these 3D hybrid structures. The bone remodeling process is carried out by an equilibrium between bone resorption produced by osteoclasts and bone mineralization mediated by osteoblasts,[52] which is initiated as early as 3−4 weeks.[53] Therefore, scaffolds so prepared by a mixture of organic (chitosan and κ-carrageenan) and inorganic (mesoporous silica nanostructures) form 3D bioactive and stable structures that are suitable to be used as osseous substitutes for bone tissue grafts.

Viability Assays. A preliminary screening of the biocompatibility was performed by using two different techniques to assay the macrophage viability. Macrophages have been demonstrated to have heightened sensibility to simvastatin.[54−56] The nonleaching components or degradation products from implantable scaffolds are a primary concern in regenerative medicine. Hence, we investigated the effects on cell viability produced by incubating the macrophage cells with the components released from highly porous scaffolds, which were previously incubated in a cell culture medium for 1, 7, and 14 days at 37 °C. The colorimetric assay (WST-1 based) employs the dehydrogenase activity to measure the mitochondrial impairment that is highly correlated with cell proliferation. In this regard, cells cultured with fluid extracts from

DOI: 10.1021/acsomega.8b03676
ACS Omega 2019, 4, 5496−5508

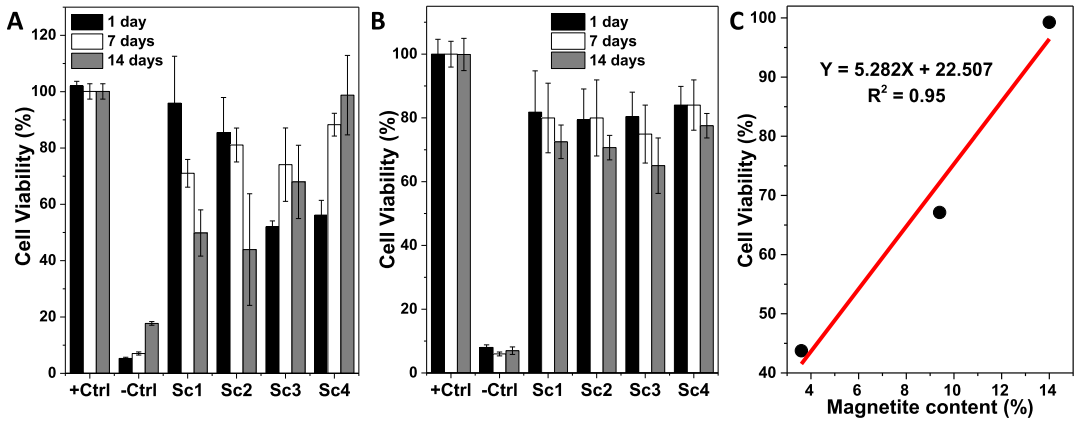

Figure 11. Cell viability studied by neutral red assay for fluid extracts corresponding to (A) plain scaffolds, (B) simvastatin-loaded scaffolds, and (C) linear relationship between the magnetite content and cell viability measured at 14 days of assay of the plain scaffolds.

plain scaffolds (no simvastatin loaded) demonstrated that their compatibility depended largely on the composition and incubation time of the scaffolds as is observed in Figure 10A. Thus, plain scaffolds showed excellent biocompatibility during the first 7 days, which was moderately decreasing over time, ranging between 73 and 61% (slightly cytotoxic) after 14 days of incubation. Therefore, the toxic effect increased as the concentration of the leached products (cross-linking agent, degradation products...) accumulated in the well. These results are perfectly comprehensible if it is taken into consideration the static conditions during cell culture assays, compared to the dynamic conditions that allowed for refreshing medium of a real scenario of a regenerative process.

The beneficial effect of simvastatin to promote bone formation after local administration has been described,[57−59] proving to be a promoter of osteoblastic activity;[44] however, its cytocompatibility properties depend strongly on the concentration when this is administrated by topical injection.[60] Thus, it will be necessary to set a critical point to perform an adequate simvastatin release profile in the site of action because its optimal therapeutic threshold is not yet determined. In this context, the effect of the simvastatin released from 3D mesoporous scaffolds was also studied.

Simvastatin incorporated within the scaffolds had a strong effect when was released to the culture medium, as is shown in Figure 10B. Its presence increased the macrophages viability over time, beyond 100% at 14 days of assay, on contrary to the patterns displayed by nonloaded scaffolds. In vitro release profiles showed that cells were exposed to a fast and an accumulative simvastatin release for at least 24 h, causing a cell proliferation inhibition. This simvastatin concentration was estimated in the range between 10 and 30 μM. However, the ability of the scaffolds to sustainably release simvastatin for a long time allowed reversing the effect observed during the first hours by increasing the viability after 7 days, except for Sc3 that showed an increase from the first day. Nevertheless, it should be considered that the simvastatin release profiles in the culture medium could greatly differ from those in PBS; therefore, it will not necessarily be reproduced in a similar way in another physiological medium or under other conditions.

To rule out the possibility that simvastatin has interfered with the cell proliferation method, a biocompatibility study using simvastatin and its soluble derivative pravastatin at different concentrations (1, 5, 10, 30, 50, and 100 μM) was also performed at exactly same conditions that previous experiments. Wells containing simvastatin and culture medium with no cells were used as a control. A dose-dependent effect on cell viability was clearly observed for pravastatin (Figure 10C), showing a proliferating effect below 5 μM. This effect on cell activity was inversely proportional to the drug concentration; the lowest tested concentration seemed to activate the growth of cells. The effect observed at high concentrations might be related to a deteriorating effect on cells by pravastatin, or just to its low solubility in the cell culture medium (pH 7.2−7.4). For its part, simvastatin exhibited the highest cell viability percentage at a concentration of 10 μM, although it also presented a proliferative effect in all of the studied concentrations, as was also observed in the simvastatin-loaded scaffolds. Hence, simvastatin did not interfere with cell proliferation at any investigated concentration. The observed trends agree with that exposed by Park[54] regarding the effects of statins on bone growth promotion, where at low concentrations, they exert a proliferating effect, whereas at higher concentrations, the proliferation is inhibited. In our study, the simvastatin released at low concentrations enhanced the RAW 267.4 macrophages cell proliferation, as we hypothesized and as other works previously showed.[55,56]

A neutral red assay was performed to complement the information regarding cell compatibility of the scaffolds. The results of the neutral red assay for both the plain and simvastatin-loaded scaffolds are given in Figure 11. The cytotoxicity of the 3D mesoporous scaffolds was expressed as the percentage of viable cells compared to control cells cultivated in a fresh medium. By testing the extracts recollected from plain scaffolds, it was observed that the cytotoxicity considerably increased for Sc1 and Sc2 at 14 days, and according to the dehydrogenase assay, on the contrary, the Sc4 sample notably increased its viability, which could be associated with the growing accumulation of leachable compounds in the well. However, we found a linear relationship at 14 days of assay between the magnetite content and cell viability in those scaffolds made from a magnetic mesoporous nanocomposite. Thus, the compatibility increased directly proportional to the amount of magnetite present in the sample as is shown in Figure 10C.

On the other hand, cells treated with fluid extracts obtained from simvastatin-loaded scaffolds proved to be noncytotoxic. It should be considered that nondynamic conditions of in vitro cell culture might exacerbate the toxic effect because in an in vivo situation, the physiological clearance would remarkably

DOI: 10.1021/acsomega.8b03676
ACS Omega 2019, 4, 5496−5508

decrease the concentration of leachable products. Furthermore, although not early toxicity was found in any case, viability never reached 100%. According to neutral red assay, the macrophage cytotoxic response was mainly restricted to the differences between each scaffold such as surface functionality, magnetite content, and probably, the magnetic NPs arrangement in the employed nanocomposites.

There are a few reports available in the literature on the cytocompatibility of the hybrid mesoporous materials with a variety of chemical compositions, where different incubation times and cell types were used.[49,61,62] In this work, two different assays have been used to evaluate the cell viability of an immortalized cell-line of murine macrophages, where they were cultivated with fluid extracts recollected from mesoporous scaffolds. In other words, cell viability was evaluated according to two different parameters: the metabolic activity by measuring the enzymatic conversion of the tetrazolium salt in the mitochondria, and the cell membrane integrity by measuring the uptake of the neutral red by living cells. Overall, the differences between both assays also depended on their features and sensitivity even when the same cell line was tested. In the WST-1 test, the increase in the mitochondrial dehydrogenase activity when macrophages were in contact with the simvastatin released from scaffolds, resulted in an increase in the number of viable cells over time. In the neutral red assay, the effect of a compound is localized in lysosomes, without affecting the mitochondria.

Thus, the scaffolds for tissue regeneration must provide an adequate environment for cell growth and proliferation. During this remodeling process, an in vivo inflammatory response has been usually observed. In this regard, RAW 264.7 cells are a murine macrophage line that displays inflammatory features similar to in vivo macrophages. Our in vitro results demonstrated that the hybrid mesoporous scaffolds containing simvastatin did not have an early cytotoxic reaction under the conditions tested, contributing to the macrophage cell proliferation. In addition, they displayed mechanical strength and a low and prolonged degradation. Further studies should be conducted in the future to explore the inflammatory response in vitro and in animal models to consider these 3D hybrid mesoporous scaffolds as therapeutic bone tissue regeneration systems.

CONCLUSIONS

In the present work, highly porous 3D mesoporous scaffolds were successfully developed by homogeneously combining bioactive, biodegradable, and easily processable polysaccharides with hybrid mesoporous silica materials. Morphological and textural properties assessed with SEM, MIP, and BET studies, including the values estimated by PoreXpert software. The composite scaffolds have a large surface area because of the presence of a vast number of interconnected pores of different sizes with an enhanced surface roughness produced by the presence of embedded mesoporous silica nanostructures. As a result of the surface chemistry and porosity of the hybrid composition of the scaffolds, large amounts of water-insoluble simvastatin were loaded in the structures, providing a sustained release for long periods that exceeded 30 days. Cytological tests did not show an adverse general response on cell viability when cells were coincubated with fluid extracts and plain scaffolds, and for simvastatin-loaded structures, a cell proliferation effect was generated over time. The biocompatibility and physicochemical properties of these scaffolds, together with their prolonged release ability, make them interesting materials for sustained release of lipophilic drugs during the bone regeneration process.

AUTHOR INFORMATION

Corresponding Author

*E-mail: y.pineiro.redondo@usc.es.

ORCID

Zulema Vargas-Osorio: 0000-0002-5220-5310
Yolanda Piñeiro: 0000-0003-4614-1629
Carlos Vázquez-Vázquez: 0000-0003-3689-4993
J. Luis Gómez-Amoza: 0000-0001-7615-6616
Francisco J. Otero Espinar: 0000-0001-9030-2253
José Rivas: 0000-0002-5059-3196

Notes

The authors declare no competing financial interest.

ACKNOWLEDGMENTS

This work was supported by the European Commission (PANA project, Call H2020-NMP-2015-two-stage, grant 686009); and the Xunta de Galicia (GPC2017/015), and partially supported by the Consellería de Educación Program for the Development of Strategic Grouping in Materials—AEMAT at the University of Santiago de Compostela under grant no. ED431E2018/08, Xunta de Galicia and Program for the Consolidation of Research Units of Competitive Reference GRC2017, grant no. ED431C 2017/22.

REFERENCES

(1) Guerado, E.; Caso, E. Challenges of Bone Tissue Engineering in Orthopaedic Patients. *World J. Orthoped.* **2017**, *8*, 87.

(2) Ghassemi, T.; Shahroodi, A.; Ebrahimzadeh, MH; Mousavian, A.; Movaffagh, J.; Moradi, A. Current Concepts in Scaffolding for Bone Tissue Engineering. *Arch Bone Jt Surg* **2018**, *6*, 90−99.

(3) Dang, M.; Saunders, L.; Niu, X.; Fan, Y.; Ma, P. X. Biomimetic Delivery of Signals for Bone Tissue Engineering. *Bone Res.* **2018**, *6*, 25.

(4) Li, Q.; Ma, L.; Gao, C. Biomaterials for in Situ Tissue Regeneration: Development and Perspectives. *J. Mater. Chem. B* **2015**, *3*, 8921−8938.

(5) O'Brien, F. J. Biomaterials & Scaffolds for Tissue Engineering. *Mater. Today* **2011**, *14*, 88−95.

(6) Du, X.; Fu, S.; Zhu, Y. 3D Printing of Ceramic-Based Scaffolds for Bone Tissue Engineering: An Overview. *J. Mater. Chem. B* **2018**, *6*, 4397−4412.

(7) Turnbull, G.; Clarke, J.; Picard, F.; Riches, P.; Jia, L.; Han, F.; Li, B.; Shu, W. 3D Bioactive Composite Scaffolds for Bone Tissue Engineering. *Bioact. Mater.* **2018**, *3*, 278−314.

(8) Oryan, A.; Sahvieh, S. Effectiveness of Chitosan Scaffold in Skin, Bone and Cartilage Healing. *Int. J. Biol. Macromol.* **2017**, *104*, 1003−1011.

(9) Saravanan, S.; Leena, R. S.; Selvamurugan, N. Chitosan Based Biocomposite Scaffolds for Bone Tissue Engineering. *Int. J. Biol. Macromol.* **2016**, *93*, 1354−1365.

(10) Prajapati, V. D.; Maheriya, P. M.; Jani, G. K.; Solanki, H. K. Carrageenan: A Natural Seaweed Polysaccharide and Its Applications" (Carbohydrate Polymers (2014) 105 (97−112). *Carbohydr. Polym.* **2016**, *151*, 1277.

(11) Zadpoor, A. A. Bone Tissue Regeneration: The Role of Scaffold Geometry. *Biomater. Sci.* **2015**, *3*, 231−245.

(12) Zhang, X.; Zeng, D.; Li, N.; Wen, J.; Jiang, X.; Liu, C.; Li, Y. Functionalized Mesoporous Bioactive Glass Scaffolds for Enhanced Bone Tissue Regeneration. *Sci. Rep.* **2016**, *6*, 1−12.

(13) Ravichandran, R.; Gandhi, S.; Sundaramurthi, D.; Sethuraman, S.; Krishnan, U. M. Hierarchical Mesoporous Silica Nanofibers as

DOI: 10.1021/acsomega.8b03676
ACS Omega 2019, 4, 5496−5508

Multifunctional Scaffolds for Bone Tissue Regeneration. *J. Biomater. Sci., Polym. Ed.* **2013**, *24*, 1988−2005.
(14) Vallet-Regí, M.; Ruiz-Hernández, E. Bioceramics: From Bone Regeneration to Cancer Nanomedicine. *Adv. Mater.* **2011**, *23*, 5177−5218.
(15) He, Y.; Luo, L.; Liang, S.; Long, M.; Xu, H. Amino-Functionalized Mesoporous Silica Nanoparticles as Efficient Carriers for Anticancer Drug Delivery. *J. Biomater. Appl.* **2017**, *32*, 524−532.
(16) Ma, G.; Zhang, J.; Chen, L.; Liu, T.; Yu, L.; Liu, X.; Lu, C. Amino-Functionalized Ordered Mesoporous Silica SBA-15, a Rapid and Efficient Adsorbent for the Adsorption of (-)-Epigallocatechin Gallate from Green Tea Extract. *RSC Adv.* **2014**, *4*, 41341−41347.
(17) Rosenholm, J. M.; Zhang, J.; Sun, W.; Gu, H. Large-Pore Mesoporous Silica-Coated Magnetite Core-Shell Nanocomposites and Their Relevance for Biomedical Applications. *Microporous Mesoporous Mater.* **2011**, *145*, 14−20.
(18) Nanaki, S.; Siafaka, P. I.; Zachariadou, D.; Nerantzaki, M.; Giliopoulos, D. J.; Triantafyllidis, K. S.; Kostoglou, M.; Nikolakaki, E.; Bikiaris, D. N. PLGA/SBA-15 Mesoporous Silica Composite Microparticles Loaded with Paclitaxel for Local Chemotherapy. *Eur. J. Pharm. Sci.* **2017**, *99*, 32−44.
(19) Bouchoucha, M.; Béliveau, É.; Kleitz, F.; Calon, F.; Fortin, M.-A. Antibody-Conjugated Mesoporous Silica Nanoparticles for Brain Microvessel Endothelial Cell Targeting. *J. Mater. Chem. B* **2017**, *5*, 7721−7735.
(20) Lashgari, N.; Badiei, A.; Ziarani, G. M. A Novel Functionalized Nanoporous SBA-15 as a Selective Fluorescent Sensor for the Detection of Multianalytes ($Fe^{3+}$and $Cr_2O_7^{2-}$) in Water. *J. Phys. Chem. Solids* **2017**, *103*, 238−248.
(21) Li, E.; Yang, Y.; Hao, G.; Yi, X.; Zhang, S.; Pan, Y.; Xing, B. Multifunctional Magnetic Mesoporous Silica Nanoagents for in Vivo Enzyme-Responsive Drug Delivery and MR Imaging. *Nanotheranostics* **2018**, *2*, 233.
(22) Vargas-Osorio, Z.; González-Gómez, M. A.; Piñeiro, Y.; Vázquez-Vázquez, C.; Rodríguez-Abreu, C.; López-Quintela, M. A.; Rivas, J. Novel Synthetic Routes of Large-Pore Magnetic Mesoporous Nanocomposites (SBA-15/Fe_3O_4) as Potential Multifunctional Theranostic Nanodevices. *J. Mater. Chem. B* **2017**, *5*, 9395.
(23) Ortolani, A.; Bianchi, M.; Mosca, M.; Caravelli, S.; Fuiano, M.; Marcacci, M.; Russo, A. The Prospective Opportunities Offered by Magnetic Scaffolds for Bone Tissue Engineering: A Review. *Joints* **2016**, *04*, 228−235.
(24) Zeng, X.; Zeng, X.; Hu, L. Q.; Xie, F.; Lan, W.; Wu, Y.; Jiang, Z. W. Magnetic Responsive Hydroxyapatite Composite Scaffolds Construction for Bone Defect Reparation. *Int. J. Nanomed.* **2012**, *7*, 3365−3378.
(25) Montero, J.; Manzano, G.; Albaladejo, A. The Role of Topical Simvastatin on Bone Regeneration: A Systematic Review. *J. Clin Exp Dent* **2014**, *6*, No. e286.
(26) Shah, S. R.; Werlang, C. A.; Kasper, F. K.; Mikos, A. G. Novel Applications of Statins for Bone Regeneration. *Natl. Sci. Rev.* **2015**, *2*, 85−99.
(27) Anbinder, A. L.; Junqueira, J. C.; Mancini, M. N. G.; Balducci, I.; Rocha, R. F. d.; Carvalho, Y. R. Influence of Simvastatin on Bone Regeneration of Tibial Defects and Blood Cholesterol Level in Rats. *Braz. Dent. J.* **2006**, *17*, 267−273.
(28) Dimitriou, R.; Jones, E.; McGonagle, D.; Giannoudis, P. V. Bone Regeneration: Current Concepts and Future Directions. *BMC Med.* **2011**, *9*, 66.
(29) Yamaguchi, A.; Katagiri, T.; Ikeda, T.; Wozney, J. M.; Rosen, V.; Wang, E. a.; Kahn, a J.; Suda, T.; Yoshiki, S. Recombinant Human Bone Morphogenetic Protein-2 Stimulates Osteoblastic Maturation and Inhibits Myogenic Differentiation in Vitro. *J. Cell Biol.* **1991**, *113*, 681−687.
(30) Riley, E. H.; Lane, J. M.; Urist, M. R.; Lyons, K. M.; Lieberman, J. R. *Bone Morphogenetic Protein-2*, 1996; Vols. *39*−*46*.
(31) Osorio, Z. V.; Pineiro, Y.; Vazquez, C.; Abreu, C. R.; Perez, M. A. A.; Quintela, M. A. L.; Rivas, J. Magnetic Nanocomposites Based on Mesoporous Silica for Biomedical Applications. *Int. J. Nanotechnol.* **2016**, *13*, 648−658.
(32) Sawkins, M. J.; Bowen, W.; Dhadda, P.; Markides, H.; Sidney, L. E.; Taylor, A. J.; Rose, F. R. A. J.; Badylak, S. F.; Shakesheff, K. M.; White, L. J. Hydrogels Derived from Demineralized and Decellularized Bone Extracellular Matrix. *Acta Biomater.* **2013**, *9*, 7865−7873.
(33) Levengood, S. K. L.; Zhang, M. Chitosan-Based Scaffolds for Bone Tissue Engineering. *J. Mater. Chem. B* **2014**, *2*, 3161.
(34) Zia, K. M.; Tabasum, S.; Nasif, M.; Sultan, N.; Aslam, N.; Noreen, A.; Zuber, M. A Review on Synthesis, Properties and Applications of Natural Polymer Based Carrageenan Blends and Composites. *Int. J. Biol. Macromol.* **2017**, *96*, 282−301.
(35) De Boulle, K.; Glogau, R.; Kono, T.; Nathan, M.; Tezel, A.; Roca-Martinez, J.-X.; Paliwal, S.; Stroumpoulis, D. A Review of the Metabolism of 1,4-Butanediol Diglycidyl Ether-Crosslinked Hyaluronic Acid Dermal Fillers. *Dermatol. Surg.* **2013**, *39*, 1758−1766.
(36) Biggs, M. J. P.; Richards, R. G.; Dalby, M. J. Nanotopographical Modification: A Regulator of Cellular Function through Focal Adhesions. *Nanomedicine* **2010**, *6*, 619−633.
(37) Bobbert, F. S. L.; Zadpoor, A. A. Effects of Bone Substitute Architecture and Surface Properties on Cell Response, Angiogenesis, and Structure of New Bone. *J. Mater. Chem. B* **2017**, *5*, 6175−6192.
(38) Bružauskaitė, I.; Bironaitė, D.; Bagdonas, E.; Bernotienė, E. Scaffolds and Cells for Tissue Regeneration: Different Scaffold Pore Sizes—different Cell Effects. *Cytotechnology* **2016**, *68*, 355−369.
(39) Rey-Aira, B.; Núñez Baz, J.; Gómez-Amoza, J. L.; Caeiro-Rey, J. R.; Luzardo Álvarez, A.; Otero-Espinar, F. J.; Blanco-Méndez, J. *Biodegradable Scaffolds Made from Natural Polysaccharides for Bone Regeneration Applications*; XII Spanish Society of Industrial Pharmacy and Galenics Congress: Barcelona, Spain, 2015.
(40) Rey-Aira, B.; Núñez Baz, J.; Gómez-Amoza, J. L.; Luzardo Álvarez, A.; Otero-Espinar, F. J.; Blanco-Méndez, J.; Guede, D.; Caeiro-Rey, J. R. *Structural Characterization of Biodegradable Scaffolds Made from Macromolecules of Natural Origin for Bone Regeneration Applications*; XIX Spanish Society of Bone Research and Mineral Metabolism Congress: Santiago de Compostela, Spain, 2014
(41) Sugawara, Y.; Kamioka, H.; Honjo, T.; Tezuka, K.; Takanoyamamoto, T. Three-Dimensional Reconstruction of Chick Calvarial Osteocytes and Their Cell Processes Using Confocal Microscopy. *Bone* **2005**, *36*, 877−883.
(42) Górniak, A.; Karolewicz, B.; Żurawska-Płaksej, E.; Pluta, J. Thermal, spectroscopic, and dissolution studies of the simvastatin−acetylsalicylic acid mixtures. *J. Therm. Anal. Calorim.* **2013**, *111*, 2125−2132.
(43) Gallagher, K. M.; Corrigan, O. I. Mechanistic Aspects of the Release of Levamisole Hydrochloride from Biodegradable Polymers. *J. Controlled Release* **2000**, *69*, 261−272.
(44) Yu, W. L.; Sun, T. W.; Qi, C.; Zhao, H. K.; Ding, Z. Y.; Zhang, Z. W.; Sun, B. B.; Shen, J.; Chen, F.; Zhu, Y. J.; Chen, D. Y.; He, Y. H. Enhanced Osteogenesis and Angiogenesis by Mesoporous Hydroxyapatite Microspheres-Derived Simvastatin Sustained Release System for Superior Bone Regeneration. *Sci. Rep.* **2017**, *7*, 1−16.
(45) Atila, D.; Keskin, D.; Tezcaner, A. Crosslinked Pullulan/cellulose Acetate Fibrous Scaffolds for Bone Tissue Engineering. *Mater. Sci. Eng., C* **2016**, *69*, 1103−1115.
(46) Li, Y.; Zhang, Z.; Zhang, Z. Porous Chitosan/Nano-Hydroxyapatite Composite Scaffolds Incorporating Simvastatin-Loaded PLGA Microspheres for Bone Repair. *Cells Tissues Organs* **2018**, *205*, 20−31.
(47) Wang, D.; Romer, F.; Connell, L.; Walter, C.; Saiz, E.; Yue, S.; Lee, P. D.; McPhail, D. S.; Hanna, J. V.; Jones, J. R. Highly Flexible Silica/chitosan Hybrid Scaffolds with Oriented Pores for Tissue Regeneration. *J. Mater. Chem. B* **2015**, *3*, 7560−7576.
(48) Yang, F.; Lu, J.; Ke, Q.; Peng, X.; Guo, Y.; Xie, X. Magnetic Mesoporous Calcium Sillicate/Chitosan Porous Scaffolds for Enhanced Bone Regeneration and Photothermal-Chemotherapy of Osteosarcoma. *Sci. Rep.* **2018**, *8*, 1−14.
(49) Ezazi, N. Z.; Shahbazi, M.-A.; Shatalin, Y. V.; Nadal, E.; Mäkilä, E.; Salonen, J.; Kemell, M.; Correia, A.; Hirvonen, J.; Santos, H. A.

DOI: 10.1021/acsomega.8b03676
ACS Omega 2019, 4, 5496−5508

Conductive Vancomycin-Loaded Mesoporous Silica Polypyrrole-Based Scaffolds for Bone Regeneration. *Int. J. Pharm.* **2018**, *536*, 241−250.
(50) Ocampo, J. I. G.; Machado de Paula, M. M.; Bassous, N. J.; Lobo, A. O.; Ossa Orozco, C. P.; Webster, T. J. Osteoblast Responses to Injectable Bone Substitutes of Kappa-Carrageenan and Nano Hydroxyapatite. *Acta Biomater.* **2018**, *83*, 425−434.
(51) Feng, W.; Feng, S.; Tang, K.; He, X.; Jing, A.; Liang, G. A Novel Composite of Collagen-Hydroxyapatite/kappa-Carrageenan. *J. Alloys Compd.* **2017**, *693*, 482−489.
(52) Florencio-Silva, R.; Sasso, G. R. D. S.; Sasso-Cerri, E.; Simões, M. J.; Cerri, P. S. Biology of Bone Tissue: Structure, Function, and Factors That Influence Bone Cells. *BioMed. Res. Int.* **2015**, *2015*, 1.
(53) Marsell, R.; Einhorn, T. A. The Biology of Fracture Healing. *Injury* **2011**, *42*, 551−555.
(54) Park, J. B. The Use of Simvastatin in Bone Regeneration. *Med. Oral Patol. Oral Cir. Bucal* **2009**, *14*, No. e485.
(55) Ahn, K. S.; Sethi, G.; Chaturvedi, M. M.; Aggarwal, B. B. Simvastatin, 3-Hydroxy-3-Methylglutaryl Coenzyme A Reductase Inhibitor, Suppresses Osteoclastogenesis Induced by Receptor Activator of Nuclear Factor-κB Ligand through Modulation of NF-κB Pathway. *Int. J. Cancer* **2008**, *123*, 1733−1740.
(56) Moon, H.-J.; Kim, S. E.; Yun, Y. P.; Hwang, Y.-S.; Bang, J. B.; Park, J.-H.; Kwon, I. K. Simvastatin Inhibits Osteoclast Differentiation by Scavenging Reactive Oxygen Species. *Exp. Mol. Med.* **2011**, *43*, 605−612.
(57) Yamashita, M.; Otsuka, F.; Mukai, T.; Otani, H.; Inagaki, K.; Miyoshi, T.; Goto, J.; Yamamura, M.; Makino, H. Simvastatin Antagonizes Tumor Necrosis Factor-alpha Inhibition of Bone Morphogenetic Proteins-2-Induced Osteoblast Differentiation by Regulating Smad Signaling and Ras/Rho-Mitogen-Activated Protein Kinase Pathway. *J. Endocrinol.* **2008**, *196*, 601−613.
(58) Ayukawa, Y.; Okamura, A.; Koyano, K. Simvastatin Promotes Osteogenesis around Titanium Implants: A Histological and Histometrical Study in Rats. *Clin. Oral Implant. Res.* **2004**, *15*, 346−350.
(59) Naito, Y.; Terukina, T.; Galli, S.; Kozai, Y.; Vandeweghe, S.; Tagami, T.; Ozeki, T.; Ichikawa, T.; Coelho, P. G.; Jimbo, R. The Effect of Simvastatin-Loaded Polymeric Microspheres in a Critical Size Bone Defect in the Rabbit Calvaria. *Int. J. Pharm.* **2014**, *461*, 157−162.
(60) Thylin, M. R.; McConnell, J. C.; Schmid, M. J.; Reckling, R. R.; Ojha, J.; Bhattacharyya, I.; Marx, D. B.; Reinhardt, R. A. Effects of Simvastatin Gels on Murine Calvarial Bone. *J. Periodontol.* **2002**, *73*, 1141−1148.
(61) Subhapradha, N.; Abudhahir, M.; Aathira, A.; Srinivasan, N.; Moorthi, A. Polymer Coated Mesoporous Ceramic for Drug Delivery in Bone Tissue Engineering. *Int. J. Biol. Macromol.* **2018**, *110*, 65−73.
(62) Xu, W.; Wang, L.; Ling, Y.; Wei, K.; Zhong, S. Enhancement of Compressive Strength and Cytocompatibility Using Apatite Coated Hexagonal Mesoporous Silica/poly(lactic Acid-Glycolic Acid) Microsphere Scaffolds for Bone Tissue Engineering. *RSC Adv.* **2014**, *4*, 13495.

DOI: 10.1021/acsomega.8b03676
ACS Omega 2019, 4, 5496−5508